

TRANSIENT DYNAMICS OF SEPARATION AND REATTACHMENT ON AN AIRFOIL AND WING AT LOW REYNOLDS NUMBERS

Connor Toppings and Serhiy Yarusevych†

Department of Mechanical and Mechatronics Engineering
University of Waterloo

200 University Avenue W, Waterloo, Ontario, Canada N2L 3G1

†syarus@uwaterloo.ca

ABSTRACT

Wind tunnel experiments are performed to investigate the stall and reattachment transients for an airfoil and wing model under conditions at which a laminar separation bubble forms on the suction surface. Direct force measurements and particle image velocimetry are employed to characterise the transient aerodynamic loading and flow field development on the models. The transient changes in operating conditions leading to stall and reattachment include changes in angle of attack at multiple pitch rates and changes in Reynolds number. The time evolution of the lift coefficient is consistent with dynamic stall at higher Reynolds numbers. Laminar separation bubble bursting and formation are associated with changes in the frequencies of the highest amplitude velocity fluctuations in the separated shear layer. Spanwise PIV measurements on the airfoil and wing models indicate that the spanwise flow development is insensitive to the type of imposed transient.

INTRODUCTION

Boundary layer separation typically leads to a decrease in the lift-to-drag ratio of lifting surfaces such as aircraft wings and turbomachinery blades. Lifting surfaces that operate at aerodynamically low chord Reynolds numbers ($Re_c < 5 \times 10^5$, Carmichael, 1981) are especially prone to suction surface boundary layer separation because the boundary layers may remain laminar into the region of adverse pressure gradient.

When the Reynolds number is sufficiently high, the laminar shear layer separating from a lifting surface transitions to turbulence, causing an increase in momentum exchange across the shear layer. If the momentum increase of the near-wall fluid is sufficient to overcome the adverse pressure gradient, the turbulent shear layer may reattach, forming a region of recirculating fluid known as a laminar separation bubble (LSB) (Tani, 1964). LSBs are sensitive to changes in adverse pressure gradient, Reynolds number, and disturbance environment, and small changes in any of these conditions may lead to a rapid LSB expansion (Gaster, 1967; Marxen & Henningson, 2011). This event is termed bursting (Gaster, 1967), and causes a substantial loss of lift and increase of drag (Tani, 1964).

Characterisation of the specific set of conditions that lead to LSB bursting has been the focus of several previous investigations under quasi-steady conditions (e.g., Gaster, 1967; Mitra & Ramesh, 2019). However, understanding the unsteady dynamics of LSB formation and bursting is prerequisite for the development of predictive models of the transient forces generated by lifting surfaces under unsteady conditions at low

Reynolds numbers. Furthermore, three-dimensional tip effects on finite span lifting surfaces lead to spanwise variations in adverse pressure gradient which may substantially influence LSB formation and bursting transients in real-world applications.

The objective of this study is to characterise the aerodynamic forces generated by a finite wing operating at a low Reynolds number during a transient change in operating conditions, and relate these forces to the flow-field development. Two types of transient changes in operating conditions are compared: changes in freestream velocity and changes in angle of attack. Direct force measurements are used to quantify the unsteady loads, while simultaneous particle image velocimetry measurements are employed to characterise the transient flow-field of the LSB.

EXPERIMENTAL METHODS

Experiments were performed in the recirculating wind tunnel at the University of Waterloo. The turbulence intensity in the empty test section is less than 0.09%. An aspect ratio 2.5 wing model of chord $c = 0.2\text{m}$ with a NACA 0018 cross-section was cantilevered vertically from the floor of the $0.62\text{m} \times 0.62\text{m}$ test section. A schematic of the model setup is presented in fig. 1. A two-dimensional airfoil model was approximated by attaching an extension to the end of the wing model (dashed line in fig. 1) so that the model spanned the entire height of the test section. The angle of attack of the wing and airfoil models was controlled through a stepper motor connected by a worm gear drive. The uncertainty of the angle of attack is estimated to be 0.06° (95% confidence). The wing model was attached to the turn table through a 6-axis JR3 30E12A4 load cell. The voltage signals from the load cell were and recorded using a 24-bit National Instruments PCI-4472 data acquisition card at a sampling rate of 10kHz. The absolute uncertainty in instantaneous lift and drag force measurements is estimated to be less than 0.2N. However, since the assumed constant bias error of the load cell does not affect comparisons between force measurements, the presented uncertainties in aerodynamic coefficients account solely for random errors in the measurements. The reference velocity used in the calculation of lift and drag coefficients was obtained from a single hot-wire anemometer located in the test section $2.75c$ upstream of the model.

To isolate the aerodynamic loads from the inertial loads acting on the load cell during pitching motions, the lift and drag forces measured in quiescent conditions were subtracted from the lift and drag forces obtained during flow measure-

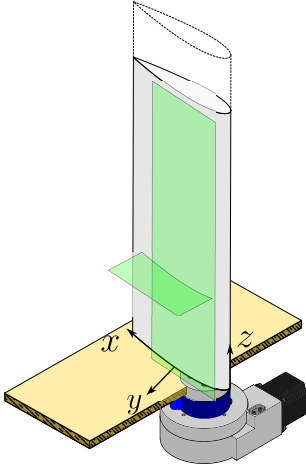


Figure 1: Model setup and definition of surface-attached coordinate system. PIV measurement planes in green.

ments. To attenuate fluctuations in the measured force coefficients caused by random noise and structural vibrations, the lift and drag coefficients were filtered using empirical mode decomposition (e.g., Rilling *et al.*, 2003). The filtering procedure used here involved subtracting the first six intrinsic mode functions (IMF) from the raw force coefficient data. Cubic spline interpolation was used to compute the signal envelope. The sifting process for each IMF was stopped when the relative tolerance between consecutive sifting results was less than 0.15 or at a maximum of 50 sifting iterations, whichever occurred first.

The wing and airfoil models were subject to two types of unsteadiness: changes in angle of attack, and changes in Reynolds number. The changes in angle of attack were performed between 10° and 13° at reduced pitch rates in the range $3 \times 10^{-5} \leq \dot{\alpha}c/2u_\infty \leq 5 \times 10^{-3}$. The time-history of the angle of attack for all pitch rates tested is shown in fig. 2. The Reynolds number was maintained at $1 \times 10^5 \pm 1.5 \times 10^3$ during the pitching motions. Changes in Reynolds number were performed between $8 \times 10^4 \leq Re_c \leq 1 \times 10^5$ by changing the wind tunnel fan speed. Time $t = 0$ is defined as the time that the turn table or wind tunnel fan was commanded to begin changing the angle of attack or Reynolds number, respectively. Temporal data are presented in terms of the convective time $D = \frac{1}{c} \int_0^t u_\infty(\tau) d\tau$, equivalent to the number of chord lengths that the freestream has travelled at time t after the beginning of the commanded pitching motion or Reynolds number change. For ensemble statistics, measurements were taken for each type of transient over 20 runs.

Planar, two-component PIV measurements were acquired during the pitching motions at reduced pitch rates of $\dot{\alpha}c/(2u_\infty) = \pm 3 \times 10^{-4}$ and $\pm 5 \times 10^{-3}$ and during Reynolds number changes between $Re_c = 8.0 \times 10^4$ and 1.0×10^5 . The PIV measurements were performed in two orthogonal planes as illustrated in fig. 1. Measurements in each plane were obtained during separate runs. The particles were illuminated with a laser light sheet with a thickness of approximately $0.01c$.

The plane tangent to and offset from the suction surface is termed the top-view plane. The laser sheet for the top-view plane was positioned parallel to the model chord and the minimum distance between the model surface and the laser sheet was 3 mm. Top-view particle images were acquired using a side-by-side arrangement of three LaVision sCMOS 5.5 megapixel cameras, operating in double-frame mode with a

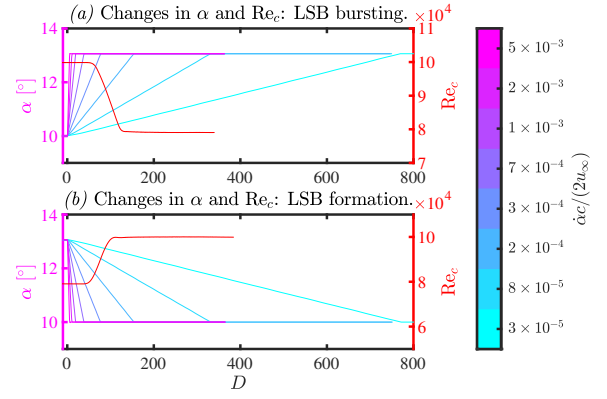


Figure 2: Controlled angle of attack and Reynolds number changes leading to LSB bursting (a) and formation (b) on the suction surface of the airfoil and wing models.

sampling frequency of 25 Hz and a laser pulse separation interval of $80 \mu\text{s}$. All three cameras were equipped with 50 mm focal length lenses with the apertures set to $f/4$. The combined field of view covers $0.03 < X/c < 0.77$ in the chordwise direction and $0 < z/c < 2.5$ in the spanwise direction. The initial and final correlation window sizes were $64\text{px} \times 64\text{px}$ and $24\text{px} \times 24\text{px}$, respectively, yielding a vector pitch of $0.002c$. A total of 250 samples were acquired during each transient pitching motion or Reynolds number change.

The PIV measurement plane normal to the span of the model is termed the side-view plane. The laser sheet for the side-view plane was positioned at $z/c = 1.5$ and $z/c = 1$ for measurements on the airfoil and wing, respectively. These locations were selected to reduce the influence of spanwise flow due to end effects on the 2-component PIV measurements. Side-view particle images were acquired using two side-by-side Photron Fastcam SA4 1 megapixel cameras in double-frame mode with a laser pulse separation interval of $60 \mu\text{s}$ at a sampling frequency of 2500 Hz. The side-view cameras were equipped with 200 mm focal length lenses with the apertures set to $f/4$. The combined field of view is $0.15 < x/c < 0.52$ and $0 < y/c < 0.7$. The initial and final correlation window sizes were $24\text{px} \times 24\text{px}$ and $16\text{px} \times 16\text{px}$, yielding a vector pitch of $0.003c$, and a total of 5457 samples were acquired during each transient pitching motion or Reynolds number change.

RESULTS AND DISCUSSION

The relationship between ensemble-averaged unsteady and quasi-steady lift coefficients of the airfoil and wing models for changes in angle of attack are examined in fig. 3. As expected, there is a reduction in the quasi-steady lift of the finite wing relative to the airfoil at a given angle of attack. For both models, there is substantial hysteresis in the lift coefficient for quasi-steady and unsteady pitching motions. The presence of a hysteresis loop for both models is characteristic of lifting surfaces operating at low Reynolds numbers (e.g., Mueller, 1985), and suggests the presence of an LSB on both models under the conditions investigated. The static stall angles for increasing angle of attack for the airfoil and wing models are 11.9° and 12.0° , respectively, and the static reattachment angles for decreasing angle of attack are 11.3° and 10.3° , respectively. The increase in the stall and reattachment angles of the wing relative to the airfoil is attributed to the reduction in effective angle of attack caused by the presence of the wing tip. The

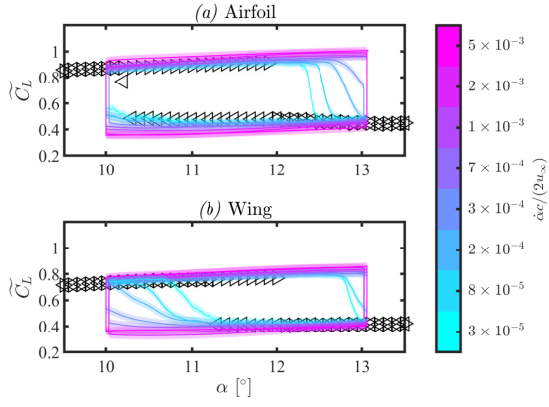


Figure 3: Quasi-steady (markers) and transient (lines) lift coefficients for pitching airfoil and wing at $Re_c = 1 \times 10^5$. \triangleright : increasing α , \triangleleft : decreasing α . Shaded areas denote uncertainty (95% confidence).

ensemble-averaged lift coefficients from the transient pitching motions exhibit an enlargement of the hysteresis loop with increasing pitch rate. At the highest pitch rates, stall and reattachment do not occur until after the final angle of attack is reached. As expected for lifting surfaces undergoing dynamic stall and reattachment, larger lift overshoots and undershoots relative to the quasi-steady lift coefficients are observed for increasing pitch rates (e.g., McCroskey, 1981; Green & Galbraith, 1995).

The time evolution of the lift coefficients for individual runs during transient pitching motions and Reynolds number changes is illustrated in fig. 4 for transients leading to LSB bursting and formation on the airfoil. Because the duration of the transient pitching motions depends on pitch rate (fig. 2), the passing of the static stall angle occurs at later times for slower pitch rates. To facilitate the comparison of lift coefficients between different cases, the data in fig. 4 are plotted against $(D - D_{ss})$ and $(D - D_{sr})$, where D_{ss} and D_{sr} are the values of D corresponding to the times when the static stall and static reattachment conditions, respectively, are passed. As the pitch rate is increased, stall occurs with a shorter delay after the passing of the airfoil's static stall condition (fig. 4a). However, the reduction in stall delay decreases as the pitch rate increases, suggesting a lower limit to the time required for stall to occur after the passage of the static stall condition, which is on the order of 10 convective time units for the airfoil. For the fastest pitch rates, substantial over- and under-shoot in the lift coefficients is observed during stall and reattachment, consistent with the dynamic stall and reattachment processes observed at higher Reynolds numbers (Kiefer *et al.*, 2022; Green & Galbraith, 1995). It is interesting to note that the lift coefficients during transient Reynolds number decreases (red lines in fig. 4a) decay nearly as fast as during the fastest pitch rates, despite the overall duration of the Reynolds number changes being approximately 80 convective time units (fig. 2a).

The lift coefficients during transients leading to LSB formation in fig. 4b display an overall trend of faster reattachment as the pitch rate is increased. However, there is considerably more variation in the time instant at which there is a rapid change in lift compared to the pitch up motions in fig. 4a. Compared to the wing, this variability is greater for the airfoil, which is attributed to the closer proximity of the static reattachment angle to the final angle of attack after pitch down motions (fig. 3a).

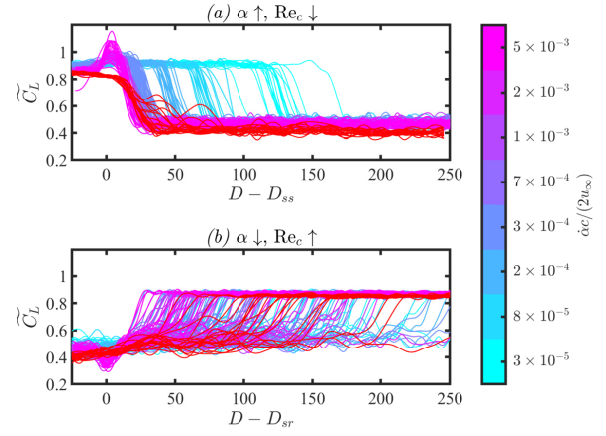


Figure 4: Lift coefficient time-history during LSB bursting (a) and formation (c) on airfoil. Shaded areas indicate uncertainty (95% Confidence). Red line: Reynolds number change at $\alpha = 10^\circ$.

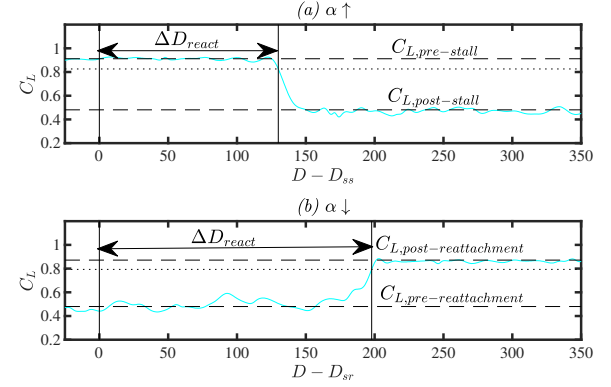


Figure 5: Definition of reaction time. Dashed lines: lift coefficients at static stall and reattachment angles; dotted line, threshold of 80% of the difference between pre- and post-stall and reattachment angles.

To quantify the variations in the time delay between the passing of the static stall or reattachment condition and the step-like change in lift coefficient indicating stall (LSB bursting) or reattachment (LSB formation), a method based on that of Le Fouest *et al.* (2021) was employed, as illustrated in fig. 5. The non-dimensional reaction delay (ΔD_{react}) is defined as the time delay between the static stall or reattachment condition and the time when the lift coefficient first crosses a threshold set at 80% of the difference between pre-stall and post stall (or post-reattachment and pre-reattachment) static lift coefficients, respectively. The same upper 80% relative threshold was used for both stall and reattachment reaction times because the relatively higher degree of lift coefficient fluctuations in the stalled state made lower thresholds less consistent for identifying the timing of the lift increase indicative of reattachment.

The computed reaction delays for all pitch rates and Reynolds number changes for the airfoil are presented in fig. 6. As the pitch rate is increased, the reaction delays for stall of the airfoil decrease asymptotically. These results largely follow the trend reported by Ayancik & Mulleners (2022) for ramp-up and sinusoidal pitching motions at Reynolds numbers spanning $7.5 \times 10^4 \leq Re_c \leq 9.2 \times 10^5$. The asymptotic decrease in reaction delay suggests that the time-evolution of the lift force is governed by the dynamic stall vortex (DSV) formation pro-

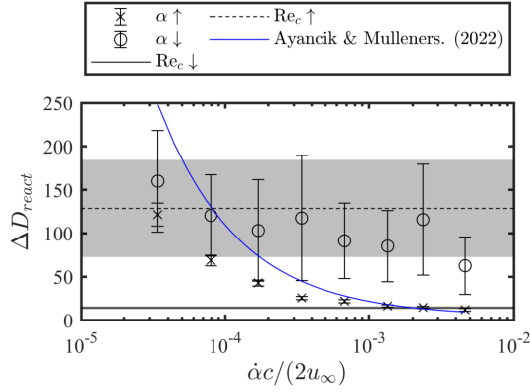


Figure 6: Reaction time delay versus pitch rate for changes in angle of attack (markers), and reaction time delay for changes in Reynolds number (horizontal lines) for airfoil. Error bars and shaded areas denote standard deviations.

cess (Ayancik & Mulleners, 2022), with the details of LSB transition having a relatively minor influence. At the highest pitch rate tested ($\dot{\alpha}c/(2u_\infty) = 5 \times 10^{-3}$), the airfoil stall reaction delay is $\Delta D_{react} = 12$.

The reaction delays for stall of the airfoil during Reynolds number changes are comparable to those of the fastest pitch rates tested, despite the duration of the Reynolds number change being longer (fig. 2). The relatively long reaction delays for the pitching motions of comparable duration ($\dot{\alpha}c/(2u_\infty) = \pm 3 \times 10^{-4}$) are likely a consequence of the fact that pitching the model involves an initial change in lift that is opposite in sense to the difference in lift between the two limiting states. For example, during a pitch up motion, the lift first increases before stall occurs (fig. 3), and this change requires additional time. However, during a decrease in Reynolds number, the lift continuously decreases up to and past the static stall Reynolds number.

In contrast to the reaction delays for stall on the airfoil, the reaction delays for reattachment on the airfoil are longer and more variable. This result is attributed to the proximity of the lower limiting angle of attack to the static reattachment angle for the airfoil at the tested Reynolds number. In such case, it is speculated that the initiation of reattachment is more sensitive to minute random perturbations in the test section environment. To investigate the influence of the particular operating conditions of the present study on the evolution of the aerodynamic loading, additional tests were performed for pitching motions between $\alpha = 9^\circ$ and 14° . In the tests with the wider separation of initial and final angles of attack (omitted for conciseness), the timing of the rapid increase in lift on the airfoil during pitch down motions was earlier and less variable, and the reaction delays for stall and reattachment largely followed the same trend as the stall reaction delays plotted in fig. 6. Thus, the substantially longer reaction delays for reattachment on the airfoil observed in the present study are a consequence of the particular operating conditions chosen.

To obtain a statistical description of LSB formation and bursting, the ensemble statistics discussed in the remainder of this paper were computed after shifting all runs by $(D_{sr} + \Delta D_{react})$ or $(D_{ss} + \Delta D_{react})$ convective time units so that the initiation or cessation of reattachment occurs at the same time during all runs for the changes in operating conditions leading to LSB formation or bursting, respectively.

Transient LSB Development

The side-view PIV configuration was used to investigate the transient development of the LSB on the suction surface of the airfoil during transient pitching motions and changes in chord Reynolds number. Figure 7 depicts instantaneous spanwise vorticity fields of the LSB on the suction surface of the airfoil for reduced pitch rates of 3×10^{-4} (fig. 7a) and -3×10^{-4} (fig. 7b). The snapshots are sequenced according to the number of convective time units offset by the reaction time ($D - D_{react}$). Prior to the LSB bursting during the increase in angle of attack (fig. 7a, $D - D_{react} = -15$), the separated laminar shear layer rolls up into discrete vortices at $x/c = 0.2$. The ensuing breakdown of these vortices leads to transition and reattachment of the flow farther downstream, as evidenced by the negative vorticity along the airfoil surface for $x/c > 0.25$. As the reaction time is approached, the trajectory of the separated shear layer moves away from the airfoil surface, and for $D - D_{react} \geq 0$, reattachment no longer occurs. The formation of the LSB during the decrease in angle of attack illustrated in fig. 7b shows that reattachment occurs for $D - D_{react} \geq 0$ once the trajectory of the separated shear layer has moved sufficiently close to the airfoil surface.

The substantial change in shear layer trajectory between reattaching and stalled conditions is expected to change the frequencies and amplitudes of amplified disturbances that lead to vortex roll-up and transition. Figure 8 presents ensemble-averaged wavelet amplitude scalograms of the wall-normal velocity fluctuations in the flow over the airfoil model sampled at $x/c = 0.25$ and the wall normal distance equal to the displacement thickness. This location is indicated by the x marker in fig. 7. The wavelet transform was performed using a Morse wavelet with a time-bandwidth product of 120. The central frequencies of disturbance amplification in the separated shear layer are approximately $fc/u_\infty = 25$ and 12 for the limiting reattaching state and the limiting stalled states, respectively. The data from the upward pitching motions (figs. 8a and 8c) indicate an increase in the amplitudes of relatively low-frequency velocity fluctuations prior to LSB bursting at $D - D_{react} = 0$. The reduction in computed peak wavelet amplitudes for $-7 < D - D_{react} < 0$ is related to the upstream movement of the location of vortex roll-up at this time (c.f. fig. 7a), which reduces the measured velocity fluctuation amplitudes at the location where the wall-normal velocity signal is extracted. In contrast to the upward pitching motions, during the decrease in Reynolds number significant low-frequency content is not observed until after $D - D_{react} = 0$. However, for the upward pitching motions and the decrease in Reynolds number, the most substantial change in the highest amplitude frequency occurs within $-5 < D - D_{react} < 5$. Similarly, during the pitch down motions and increase in Reynolds number, the most substantial changes in the highest amplitude frequency occur within a relatively short time interval before $D - D_{react} = 0$.

Spanwise Flow Development

The spanwise progression of LSB formation and bursting was investigated using the top-view PIV configuration. Tests of the airfoil and wing models are compared in this section to understand the influence of end effects on the transient flow development. Instantaneous snapshots of streamwise velocity for the airfoil and wing models in the limiting steady-state conditions for the pitching motions and Reynolds number changes are presented in fig. 9. Note that the airfoil model extends across the entire test section to $z/c = 3$. In the limiting attached flow state where an LSB forms on the suction

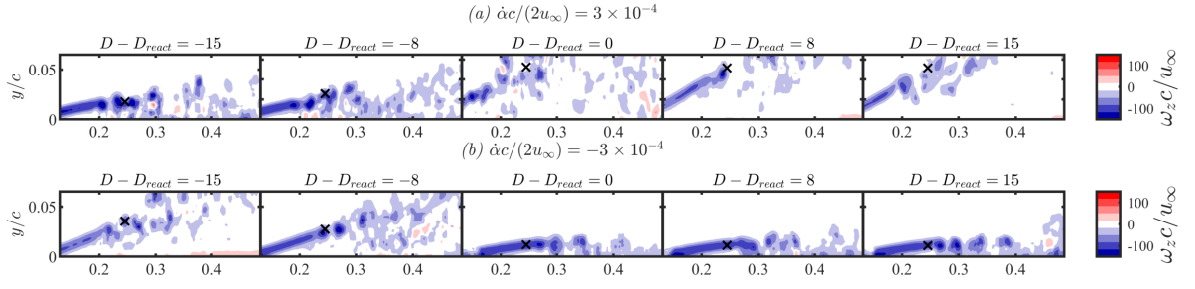


Figure 7: Contours of spanwise vorticity during pitch up (a) and pitch down (b) motions for airfoil at $\dot{\alpha}c/(2u_\infty) = \pm 3 \times 10^{-4}$. X marker indicates location of velocity fluctuations sampled for wavelet analysis.

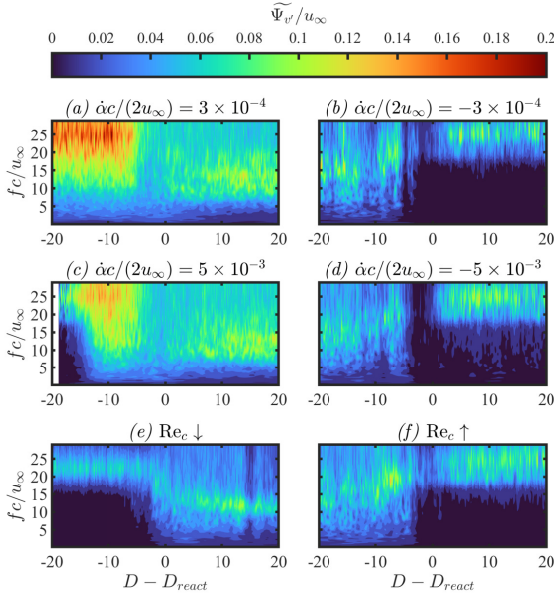


Figure 8: Contours of ensemble-averaged wavelet amplitude during LSB bursting (a,c,e) and formation (b,d,f).

surface at $\alpha = 10^\circ$ (figs. 9a and 9d), transition to turbulence occurs at approximately $X/c = 0.30$ on both the airfoil and wing models due to roll-up of the separated shear layer into spanwise vortices that appear in the snapshots as spanwise ridges of increased streamwise velocity. A corner separation is also present in the top-view measurements for $x/c \geq 0.2$, at $z/c = 0$. In the limiting stalled flow state at $\alpha = 13^\circ$ and $Re_c = 1.0 \times 10^5$ (figs. 9b and 9e), a region of turbulent reverse flow occurs for $X/c \geq 0.2$, indicating massive separation of the boundary layer. On the wing (fig. 9e), boundary layer separation is suppressed near the wing tip ($z/c = 2.5$) due to downwash from the wing tip vortex. The spanwise flow development in the limiting stalled state at $\alpha = 10^\circ$ and $Re_c = 8.0 \times 10^4$ (figs. 9c and 9f) is similar to that at the higher angle of attack and Reynolds number, although the higher velocities in the recirculation region indicate that the shear layer trajectory is closer to the model surface at the lower Reynolds number.

To illustrate the temporal development of the recirculation region on the wing and airfoil models, the minimum streamwise velocity across the chordwise (X) extent of the top view PIV field of view was obtained from the ensemble of measurements aligned by reaction time and is presented in figs. 10 and 11 for transients leading to LSB bursting and formation,

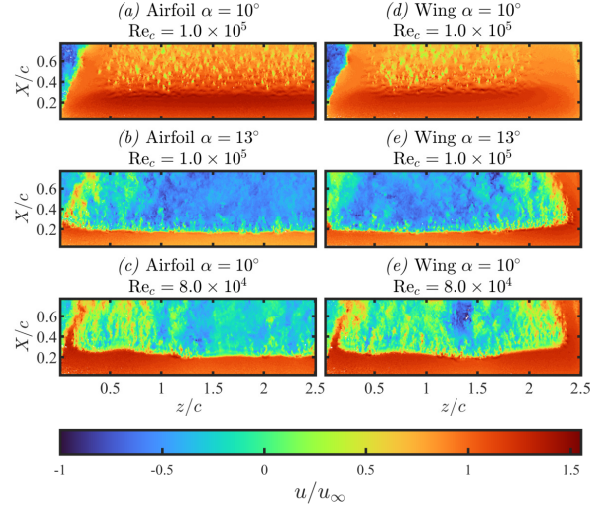


Figure 9: Streamwise velocity contours in steady conditions measured by top-view PIV configuration.

respectively.

During LSB bursting on both the airfoil and the wing (fig. 10), reverse flow appears first at $z/c = 0.5$, indicating that LSB bursting occurs first at this location. On the airfoil model, which is symmetric about the centre plane of the test section, there is also an indication of early LSB bursting at $z/c = 2.5$ for the pitching motion cases (figs. 10a and 10c). The bias of the onset of reverse flow towards $z/c = 0$ in fig. 10e during the decrease in Reynolds number is likely due to the sensitivity of the location at which the separated shear layer intersects the measurement plane to minute misalignments of the laser sheet. On the wing during LSB bursting (figs. 10b, 10d and 10f) there is a more substantial delay in the onset of reverse flow near the wing tip, consistent with the expected reduced adverse pressure gradient near the wing tip leading to delayed LSB bursting in this region. Overall, the top view PIV measurements during LSB bursting transients show qualitatively similar spanwise progressions of the recirculating flow region for each type of model, regardless of type of change in operating conditions. Similarity in spanwise flow development across different types of changes in operating conditions for each model is especially evident for the transients leading to LSB formation in fig. 11, where the initiation of reattachment is relatively more uniform in the spanwise direction compared to the cessation of reattachment. A comparison of wavelet amplitude scalograms in fig. 8 to the top-view PIV results for the airfoil in figs. 10 and 11 indicates that the onset or cessation of massive separation coincides with a distinct decrease or in-

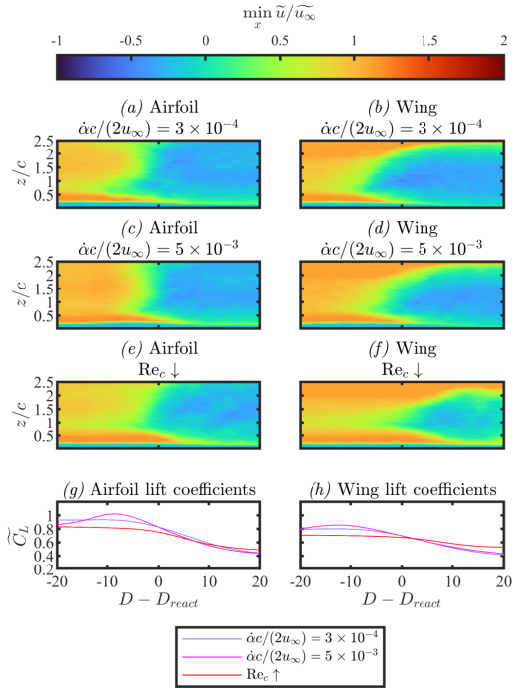


Figure 10: Contours of minimum ensemble-averaged streamwise velocity during LSB bursting.

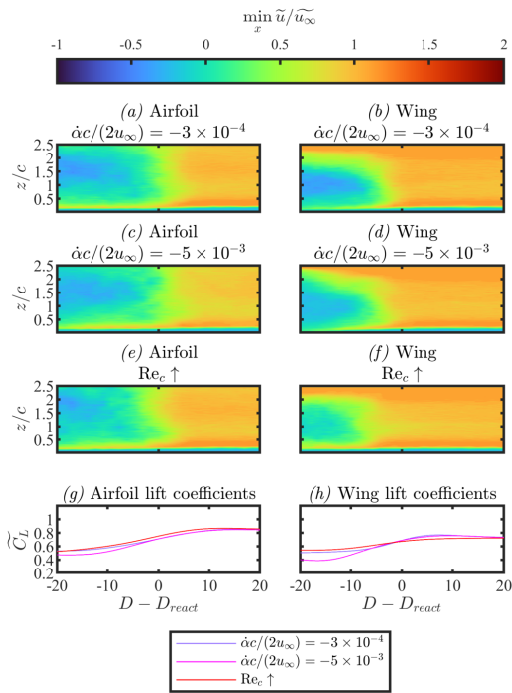


Figure 11: Contours of minimum ensemble-averaged streamwise velocity during LSB formation.

crease, respectively, in the frequencies of the highest amplitude velocity fluctuations.

CONCLUSION

The lift force on a wing and airfoil model at aerodynamically low Reynolds numbers was measured during transient

changes in angle of attack and Reynolds number. Flow development during the transients was investigated in two orthogonal PIV measurement planes. Consistent with the results of previous studies of pitching airfoils at higher Reynolds numbers, the reaction time between the passing of the static stall angle and loss of lift decreased asymptotically to a value of less than 10 convective time units as the pitch rate was increased. Thus, when the limiting operating conditions are sufficiently separated from the static stall conditions, the time evolution of the lift coefficient likely becomes governed by DSV formation rather than LSB dynamics. Despite the relatively long duration of the transient change in Reynolds number leading to LSB bursting, the reaction time for the Reynolds number change was comparable to pitching motions of substantially shorter duration. The wavelet analysis used to characterise the frequencies of disturbances in the separated shear layer during the transients revealed a distinct change in the highest amplitude frequencies in conjunction with the onset or cessation of massive separation. The spanwise PIV measurements indicated qualitatively similar spanwise expansion and contraction of the region of massive separation during LSB bursting and formation, respectively, regardless of the nature of the imposed transient change in operating conditions.

REFERENCES

- Ayancik, Fatma & Mulleners, Karen 2022 All you need is time to generalise the Goman–Khrabrov dynamic stall model. *Journal of Fluid Mechanics* **942**, R8.
- Carmichael, B. H. 1981 Low Reynolds Number Airfoil Survey. *Tech. Rep.* NASA CR-165803. Low Energy Transportation Systems, Capistrano Beach, CA.
- Gaster, M 1967 The Structure and Behaviour of Laminar Separation Bubbles. *Tech. Rep.* Reports and Memoranda 3595. Aeronautical Research Council, London.
- Green, R. B. & Galbraith, R. A. McD. 1995 Dynamic recovery to fully attached aerofoil flow from deep stall. *AIAA Journal* **33** (8), 1433–1440.
- Kiefer, Janik, Brunner, Claudia E., Hansen, Martin O.L. & Hultmark, Marcus 2022 Dynamic stall at high Reynolds numbers induced by ramp-type pitching motions. *Journal of Fluid Mechanics* **938**, 1–22.
- Le Fouest, Sébastien, Deparday, Julien & Mulleners, Karen 2021 The dynamics and timescales of static stall. *Journal of Fluids and Structures* **104**, 103304.
- Marxen, Olaf & Henningson, Dan S. 2011 The Effect of Small-Amplitude Convective Disturbances on the Size and Bursting of a Laminar Separation Bubble. *Journal of Fluid Mechanics* **671**, 1–33.
- McCroskey, W J 1981 The phenomenon of dynamic stall. *Tech. Rep.* NASA-TM-81264. NASA Ames Research Center, Moffat Field, CA.
- Mitra, Abhijit & Ramesh, O. N. 2019 New Correlation for the Prediction of Bursting of a Laminar Separation Bubble. *AIAA Journal* **57** (4), 1400–1408.
- Mueller, Thomas J. 1985 The influence of laminar separation and transition on low Reynolds number airfoil hysteresis. *Journal of Aircraft* **22** (9), 763–770.
- Rilling, Gabriel, Flandrin, Patrick & Goncalves, Paulo 2003 On empirical mode decomposition and its algorithms. In *IEEE-EURASIP workshop on nonlinear signal and image processing*, , vol. 3, pp. 8–11.
- Tani, Itiro 1964 Low-speed flows involving bubble separations. *Progress in Aerospace Sciences* **5**, 70–103.